nature communications

Article

https://doi.org/10.1038/s41467-025-63558-0

Anthropogenic forcing drives equatorward migration of heatwave locations across continents

Received: 20 March 2025

Accepted: 22 August 2025

Published online: 02 September 2025

Check for updates

Juan Feng[1,2] ✉, Jiaxin Li[1], Fei-Fei Jin[3,4], Sen Zhao[3] & Jianping Li[5,6] ✉

Heatwaves have increased in frequency, intensity, duration, and spatial extent, posing a serious threat to socioeconomic development, natural ecosystems and human health worldwide. Assessments of trends in heatwave locations (HWL) have been hindered by the distinct regional characteristics of heatwaves across continents. Here we identify a consistent striking equatorward migration in the average latitudinal location of heatwaves occurrence over the period 1979–2023 based on various datasets. The trends of HWL in each hemisphere illustrate equatorward migration at a rate of approximately one degree of latitude per decade, which falls well into the extent of the estimated rate in the observed intertropical convergence zone contraction and the contrast in soil moisture between tropics and subtropics. Our analyses suggest that anthropogenic contribution plays a dominant role in the equatorward trends. The equatorward migration, which has already occurred and is projected to continue in future scenarios, highlights that the risk of damages and disasters caused by heatwaves may increase at lower latitudes.

Heatwaves, defined as periods of consecutive days with anomalously high temperatures, are among the most widespread and recurrent extreme weather events[1,2]. Heatwave-related health impacts are among the most significant and immediate threats to human health from climate change[3]. The discernible increase in the severity and devastation of heatwaves has resulted in catastrophic impacts across the globe, including America, Australia, South Asia, western Europe, China, South America, and West Africa[4–9].

The characteristics, i.e., intensity, frequency, duration, and spatial extent, of heatwaves have drawn much attention in recent years. There is a general consensus that the intensity, duration, and frequency of heatwaves have increased both regionally and globally[10–12], and that heatwaves can occur in all seasons of the year[13–15]. Concurrently, in terms of global atmospheric circulation changes, the Hadley circulation has expanded poleward in recent decades[16], contributing to the poleward shifts of subtropical arid zone[17] and tropical cyclones[18]. Meanwhile, the width of the intertropical convergence zone (ITCZ) has narrowed[19] and the deep convection zone contracted[20], leading to the swing in the subtropical jet[20] and rain-band[21]. These significant migrations in large-scale circulations could impact the occurrence of heatwaves and provide a basis for hypotheses regarding changes in latitudinal heatwave locations (HWL). However, variations in latitudinal HWL, particularly from a global perspective, may have been overlooked; this inhibits a comprehensive understanding of how the locations of heatwaves have changed in order to better assess the variations in and impacts of heatwaves. In this study, we examine recent global-scale changes in HWL over the past four decades based on multiple datasets. We find that the HWL exhibit significant equatorward shifts in both hemispheres, which are in accordance with the systematic

[1]State Key Laboratory of Remote Sensing Science, Faculty of Geographical Science, Beijing Normal University, Beijing, China. [2]Beijing Engineering Research Center for Global Land Remote Sensing Products, Faculty of Geographical Science, Beijing Normal University, Beijing, China. [3]Department of Atmospheric Sciences, School of Ocean and Earth Science and Technology (SOEST), University of Hawaii at Mānoa, Honolulu, HI, USA. [4]International Pacific Research Center, SOEST, University of Hawai'i at Mānoa, Honolulu, HI, USA. [5]Frontiers Science Center for Deep Ocean Multi-spheres and Earth System/Key Laboratory of Physical Oceanography/Academy of the Future Ocean, Ocean University of China, Qingdao, China. [6]Laoshan Laboratory, Qingdao, China.
✉e-mail: fengjuan@bnu.edu.cn; ljp@ouc.edu.cn

environmental changes, including contraction of ITCZ and contrast of soil moisture between tropics and subtropics. Simulations reflect the anthropogenic forcing plays a more dominant role in the observed equatorward migration of HWL than natural variability.

Results

Observed equatorward migration in HWL

Here, we consider the 45 yr period of 1979–2023, corresponding to the satellite post era in which most atmospheric reanalysis products are available. The heatwave frequency differences based on the daily maximum 2-m temperature (T_{max}) from ERA5[22] between the last and first 20 years over this period clearly increase over most continents across the globe (Fig. 1a). The increase is greater at low latitudes than at high latitudes, especially for the lower latitudes of Africa, Arabian Peninsula, East Asia, North America, and South America. When the annual-mean latitude of HWL is calculated in the Northern and Southern hemispheres (red lines in Fig. 1b, c), there are evident and statistically significant equatorward trends of 12.66 and 11.20 km per year (~1° latitude per decade) in the Northern and Southern hemispheres, respectively. This migration is consistently observed even if the intensity of heatwave events (i.e., the averaged intensity, the maximum intensity, and the accumulated intensity) is considered (Supplementary Fig. 1), indicating that this migration is not due to local change in the spatial intensity of heatwaves. In addition, the latitudinal distribution of heatwave frequency trends at the lower, middle, and high latitudes are examined to detect whether this migration is dominated by certain latitude belt. Increased frequency of heatwave events is observed in all latitude belts, however, with the largest increase for belt 10°S-10°N (Supplementary Fig. 2). And the frequency increases over belts 30°-10°S and 10°-30°N are greater than those over 50°-30°S and 30°-50°N.

The equatorward migrations of HWL in both hemispheres are further examined based on multisource datasets with various resolutions, including the CFSR[23], MERRA2[24], NCEP[25] and Berkeley Earth[26] temperature datasets. Although certain differences exist in the exact trend amplitudes and their statistical power, consistent significant equatorward migration in both hemispheres is observed (red bars in Fig. 1b, c), suggesting the robustness of the migration towards the tropics.

Considering that the daily mean 2-m temperature (T_{mean}) is also widely used to characterize heatwave activity[27–30], the migration of HWL based on T_{mean} is further examined. When this is performed, similar variability and significant trends are found in the annual-mean time series (blue lines in Fig. 1b, c), with even greater rates of 16.45 and 13.55 km per year for the Northern and Southern hemispheres, respectively. Moreover, the greater amplitudes of the T_{mean} based trend than those of the T_{max} trend in both hemispheres are consistent across various datasets (blue bars in Fig. 1b, c), implying a similar trend in the night-time temperature. This equatorward migration is also obtained across different seasons, although it shows different trend rates and significant intervals (Supplementary Fig. 3), indicating that there is no seasonal dependence in the equatorward migration of HWL. The different trends in HWL among seasons may be due to the impacts resulting from the complicated seasonal dependence and cycles of various climatic variabilities[31,32].

The regional contributions to the hemispheric trends from each continent exhibit pronounced equatorward migrations, which are consistently observed across most datasets (Fig. 1d–h), although certain differences exist in the regional trend rates. This result suggests that the migration is a global phenomenon rather than dominated by regional climatic variability. These regional differences are likely due in part to different regional responses to interannual to multidecadal

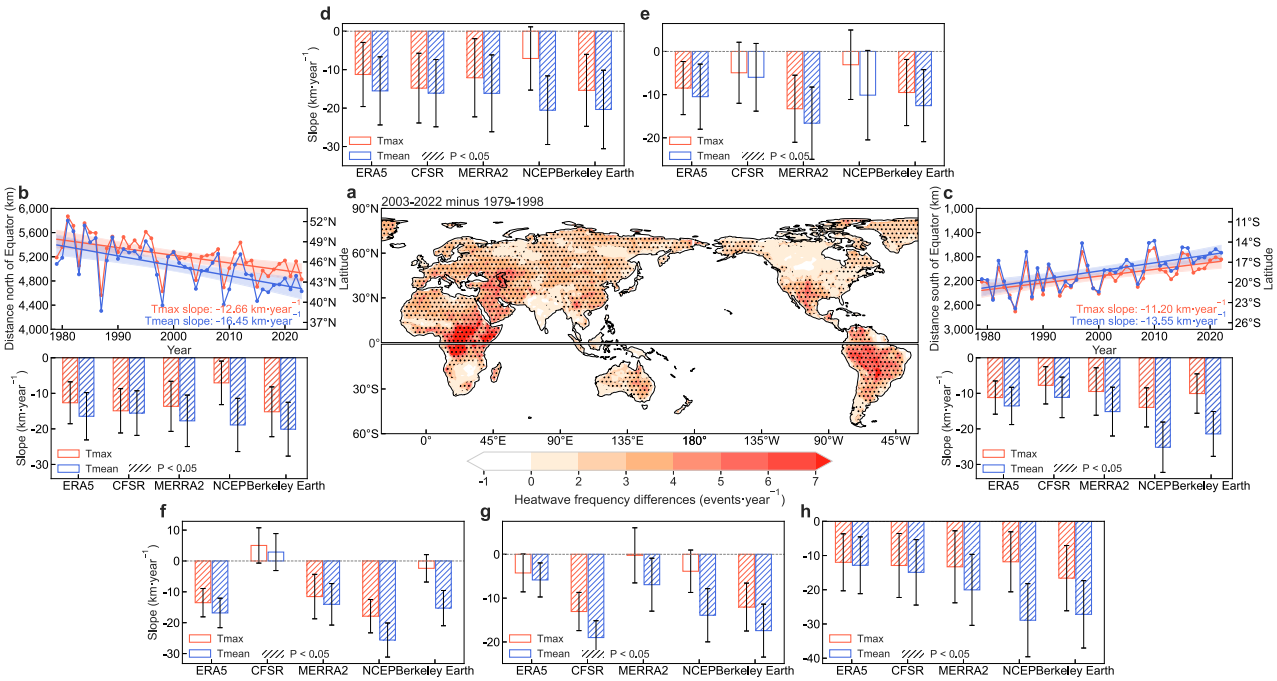

Fig. 1 | Equatorward migration of the latitude of heatwave locations (HWL). **a** Spatial distribution of annual-mean heatwave frequency differences (events year^{-1}) between periods 2003-2022 and 1979-1998 based on the EAR5. Annual-mean are taken over January-December in the Northern Hemisphere and July-June in the Southern Hemisphere. Dotted areas indicate statistical significance at the 0.05 level. **b**, **c** Time series (upper) and trends (below) of annual-mean latitude of HWL calculated from the ERA5 (lines) and from the ERA5, CFSR, MERRA2, NCEP and Berkeley Earth datasets (bars) based on daily maximum 2-m temperature (T_{max}, red) and daily mean 2-m temperature (T_{mean}, blue) in the Northern (**b**) and Southern (**c**) hemispheres, respectively. Linear trend lines are shown with their 95% two-sided confidence intervals (shaded). Error bars represent the 95% confidence interval of the slope. Negative slopes represent equatorward migration. The *y*-axis in (**c**; upper) increases downwards. **d**-**h** As in (**b**; below), but for the regional trends of annual-mean latitude of HWL for each continent over the Eurasia-North Africa (**d**), North America (**e**), South Africa (**f**), Australia (**g**) and South America (**h**) separated by the equator. The Eurasia-North Africa and North America are divided by the Bering Strait.

natural variabilities[33–35]. In the Northern Hemisphere, both Eurasia-North Africa and North America contribute significantly to the hemispheric HWL equatorward trend, which could be consistently established from ERA5, MERRA2, and Berkeley Earth datasets with an even greater amplitude over Eurasia-North Africa (Fig. 1d). The equatorward trend is statistically insignificant from CFSR and NCEP datasets over North America (Fig. 1e). A comparison of the trend amplitudes across different datasets, i.e., 4 out of 5 datasets except for MERRA2, reveals that the contribution from Eurasia-North Africa to the Northern Hemisphere trend is greater than that from North America. With respect to the Southern Hemisphere, the South American continent is an essential contributor to the hemispheric trend, which is consistent in the five datasets (Fig. 1h), with a relatively lower rate from Australia. The trend is negative but insignificant based on T_{max} from ERA5, MERRA2 and NCEP over Australia (Fig. 1g). The equatorward trend is insignificant based on T_{max} from Berkeley Earth, and the CFSR data show positive trends in both T_{max} and T_{mean} over South Africa (Fig. 1f).

Physical processes contribute to the equatorward migration of HWL

The formation and location of heatwaves, which determine when and where HWL occurs, are modulated by changes in the environmental background. Soil moisture-temperature feedbacks are considered to be a pivotal factor driving increases in heatwaves[36–38]. Reduced soil moisture (Supplementary Fig. 4a) limits evapotranspiration, resulting in decreased cloud cover (Supplementary Fig. 4b), leading to increased surface air temperatures by altering solar radiation input (Supplementary Fig. 4c) and shifting surface energy conversion from latent to sensible heat fluxes[38]. The consistency between changes in soil moisture (cloud cover, short-wave radiation) and heatwaves (Fig. 1a) is corroborated by high field correlation coefficients, exceeding −0.48 (−0.49, 0.58) ($P < 0.001$) across continents. Therefore, we examine the relationship between the HWL latitude and soil moisture (Fig. 2a). Significant positive correlations are observed at lower latitudes, while at higher latitudes in Africa, Asia, and North America, negative correlations are observed. This implies that decreased soil moisture at lower latitudes, increased soil moisture at higher latitudes, or both, could be expected to link an equatorward migration of the HWL. Accordingly, the difference of soil moisture between tropics and subtropics (SMD) is defined (see Methods) to evaluate its connection with HWL latitude. The relationship between SMD and HWL latitude show significant correlations with coefficients of 0.48 and 0.79 for the Northern and Southern hemispheres (Fig. 2b, c), respectively. That is a weakened contrast in soil moisture between tropics and subtropics would link with an equatorward shift of the HWL, which is consistent with the observed trends in them. The role of changes in soil moisture in the migration of HWL is further verified by simulations from the Coupled Model Intercomparison Project Phase 6 (CMIP6) and the Community Earth System Model version 1 (CESM1) Large Ensemble Simulations (CESM1 LES)[39] (Supplementary Table 1). Significant negative relationships are detected between HWL latitude−SMD correlations and SMD trend in both hemispheres (Fig. 2d, e). This relation suggests that models with a more pronounced weakening of SMD tend to exhibit a stronger statistical linkage between the SMD and HWL latitude. However, the relationship is insignificant when using the trend of HWL latitude as the independent variable (Supplementary Fig. 5), supporting the role of SMD in impacting the changes of HWL latitude.

Moreover, the magnitude of equatorward migration of HWL lies within the range of ITCZ contraction rate[40], or the deep tropics squeeze[20]. This allows for the hypothesis that there is a link between the equatorward migration of HWL and the contraction of the ITCZ. This connection is demonstrated by calculating the correlations between the annual-mean time series of ITCZ area[19,41] and HWL latitude. Significant correlations are obtained, with coefficients exceeding 0.35 ($P < 0.05$) in both hemispheres for both the raw and detrended data, supporting the relationship between changes in ITCZ area and HWL latitudes. This connection is further reflected in their relationship with the static stability for the close linkage between the ITCZ area and atmospheric instability (Fig. 3). The HWL latitude shows significant negative correlations with static stability in the tropics, while with significant positive correlations in the mid-latitudes (Fig. 3a). This indicates an increase in the static stability in the tropics, or a decrease in the static stability in the mid-latitudes, or both, would induce an equatorward shift of the HWL. The relationship between the static stability and ITCZ area is similar to that with the HWL. Namely, the contraction of ITCZ is expected to result in increased (decreased) static stability in the tropics (mid-latitudes) (Fig. 3b), which would favour for the HWL to migrate towards the equator. Meanwhile, significant negative relationships are detected between the connection of ITCZ area–HWL latitude and trend of ITCZ area in both CMIP6 and CESM1 LES simulations (Fig. 3c, d). This result indicates that a greater narrowing trend in ITCZ area is expected to associate with a more intense connection between the HWL latitude and ITCZ area, whereas not the case for the opposite situation (Supplementary Fig. 6).

In summary, the observed changes in soil moisture and ITCZ area support that the global migration of HWL towards the tropics is being modulated by systematic environmental changes.

Detecting natural and external impacts

El Niño–Southern Oscillation (ENSO) is the most prominent form of climate variability in tropical air–sea coupled systems and plays an important role in modulating regional heatwaves[7,35,42], which may impact the equatorward trends in HWL identified here. The contribution from ENSO is verified by regressing the HWL time series onto the ENSO variability. When the ENSO variability is reduced, the amplitude of the hemispheric migration rates slightly increases based on both T_{max} and T_{mean} (Fig. 4a, b). The limited impacts of ENSO on the HWL trend are supported by few changes in the reduced amplitude rates of ENSO across different datasets (Supplementary Fig. 7). The role of ENSO in modulating the position of HWL based on both T_{max} and T_{mean} is further established by examining the irrespective effects of El Niño and La Niña events. During El Niño events, the average position of HWL in the Northern Hemisphere shifts southwards (Fig. 4c), and a northwards shift is found in the average position of HWL in the Southern Hemisphere (Fig. 4d). That is, the average HWL latitudes in both hemispheres all are shifted towards the equator during El Niño events. The average positions of HWL are away from the equator for both the Northern and Southern hemispheres during La Niña events (Fig. 4c, d). The average magnitude of the HWL shift is greater during El Niño events than during La Niña events, revealing the asymmetric effects of ENSO warm and cold events on HWL. However, the shifts in HWL during both El Niño events and La Niña events are considerable within events and statistically insignificant, suggesting that natural ENSO variability is unlikely to play a substantial role in determining the equatorward migration of HWL.

The potential contributions from the internal variabilities occurring on interdecadal or longer time scales still remain; however, quantifying the possible impact using a relatively short record is difficult. Here, we analyse simulations from the CMIP6, which use historical simulations (with 32 models), historical simulations forced by natural forcing of solar variability and volcanic eruption (with 12 models), and historical greenhouse gas (GHG) forcing (with 12 models) to illustrate all-forcing, with only natural forcing (hist-nat) and GHG forcing (hist-GHG) including situations (Fig. 5). Considering that HWL based on T_{max} and T_{mean} shows consistent variations, only the results based on T_{max} from the experiments are displayed below. We find that the multimodel ensemble (MME) hemispheric rates of HWL display statistically significant equatorward trends in both hemispheres in the historical (orange lines in Fig. 5a, b, and Supplementary Fig. 8) and hist-GHG experiments (green lines in Fig. 5a, b, and Supplementary Fig. 9)

https://doi.org/10.1038/s41467-025-63558-0

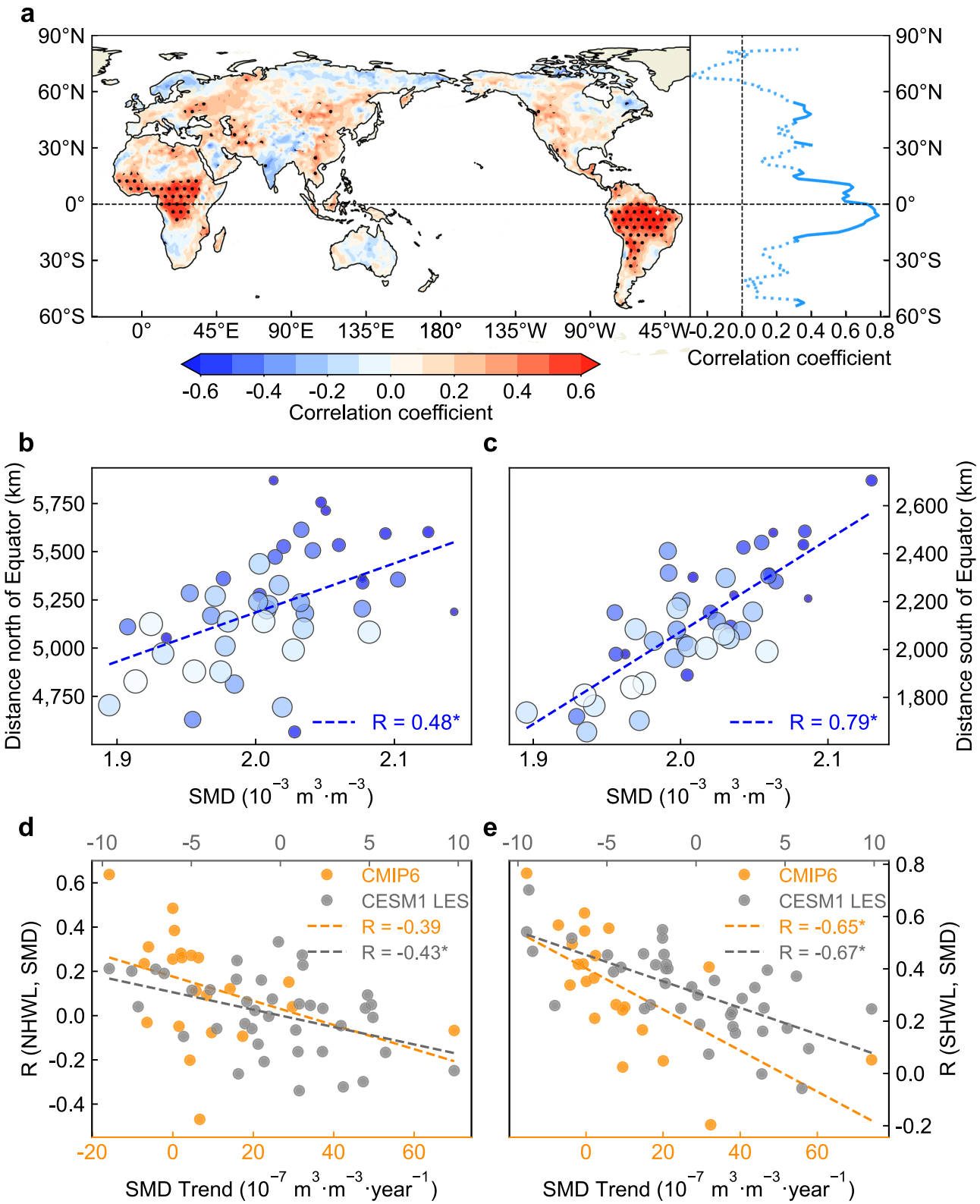

but with relatively smaller magnitudes in the historical simulations of the Northern Hemisphere. In contrast, the trends are statistically insignificant in the hist-nat experiment, although the trends are still negative in both hemispheres (blue lines in Fig. 5a, b, and Supplementary Fig. 10). As anthropogenic forcing is not included in the hist-nat simulations, the identified equatorward migration of HWL in both hemispheres is largely not driven by internal climate variability. In addition, the effect of a large volcanic eruption on HWL is detected, showing an obvious poleward shift in both hemispheres under the impacts of Mount Pinatubo in the historical and hist-nat experiments (red triangles in Fig. 5a, b). Moreover, similar equatorward trends and poleward shifts accompanied by volcanic eruption are detected in the CESM1 LES (purple lines in Fig. 5a, b, and Supplementary Fig. 11), highlighting the limited role of natural variability in impacting the equatorward shift in HWL. The above results, which are based on different experiments, establish that anthropogenic contributions play a

Fig. 2 | Physical process of soil moisture change contributes to the equatorward migration of heatwave locations (HWL). a Spatial distribution of correlations between the time series of annual-mean latitude of HWL and soil moisture, and its zonal-mean profile. Annual-mean are taken over January-December in the Northern Hemisphere and July-June in the Southern Hemisphere. Dotted areas and solid line indicate statistical significance at the 0.05 level. **b**, **c** Scatterplot and linear fit of the soil moisture difference (SMD) against the HWL latitude in the Northern (**b**) and Southern (**c**) hemispheres calculated from ERA5; with correlation coefficients shown in the bottom right corner, the asterisk indicates statistical significance at the 0.05 level. The diameter and colour of the bubble represent the sequence of years, the larger and lighter-coloured bubbles indicate the later of the year. **d**, **e** As in (**b**-**c**) but for the intermodel scatterplot and linear fit of the SMD trends ($m^3\ m^{-3}\ year^{-1}$) against the correlations between SMD and HWL latitude in the Northern (**d**; NHWL) and Southern (**e**; SHWL) hemispheres calculated from CMIP6 (referenced to the bottom *x*-axis) and CESM1 LES (referenced to the top *x*-axis) historical simulations. The CMIP6 models are selected based on their normalized root-mean-square error relative to ERA5; the specific models used are listed in the Supplementary Table 1.

more important role in determining equatorward migration than does natural variability.

Future HWL shift under global warming

A narrowing of the ITCZ[19] and a strengthened soil mositure-temperature feedback[38] are expected as the climate warms, and a concomitant continued equatorward migration of HWL is projected in the shared socioeconomic pathways 3-7.0 and 5-8.5 scenarios (SSP3-7.0 and 5-8.5) of CMIP6 (Fig. 5c, d), providing further evidence of their possible linkages. The HWL trends, have already occurred, contributing to the average position of annual-mean HWL exhibiting equatorward shifts of 2.16° and 2.64° (latitude of HWL averaged over 2005–2014 minus 1979–1988) in the Northern and Southern hemispheres (green bars in Fig. 5c, d), respectively. A relatively small equatorward shift is simulated in the CMIP6 historical experiment in the Northern Hemisphere (1.76° vs. 2.16°; orange bar in Fig. 5c), whereas a similar shift is reproduced in the Southern Hemisphere (2.69° vs. 2.64°; orange bar in Fig. 5d). Compared with the historical simulated HWL trend, a greater equatorward migration amplitude is projected in most (17 out of 18 models) of the CMIP6 models during the period 2065–2100 in the SSP3-7.0 and SSP5-8.5 scenarios. Correspondingly, the differences between the average HWL latitudes during the backmost and beginning ten years of the period from 2065 to 2100 are 4.54°/5.00° and 4.36°/5.11° for the Northern and Southern hemispheres, respectively, showing much greater meridional shifts in the SSP3-7.0 (pink bars in Fig. 5c, d)/SSP5-8.5 (blue bars in Fig. 5c, d) projections than in the historical simulation. Compared with those in the SSP3-7.0 scenario (red stars and pink bars in Fig. 5c, d), the magnitudes of the equatorward shifts in HWL and the simulated MME rates in both hemispheres are greater in SSP5-8.5 (blue stars and bars in Fig. 5c, d), which is consistent with the fact that the SSP5-8.5 scenario corresponds to higher GHG concentrations. The projected future rate of HWL equatorward migration over equal time intervals (2065–2100 vs. 1979–2014) is much greater than that in the historical simulations, which is smaller than in the observations in the Northern Hemisphere, suggesting that the trend rate of HWL towards the equator may obviously increase under the future SSP3-7.0 and SSP5-8.5 scenarios in the Northern Hemisphere. Furthermore, the equatorward migration of HWL in both hemispheres, as simulated by CESM1 LES, displays similar characteristics in both the historical period (grey stars and purple bars in Fig. 5c, d) and the RCP8.5 scenario (grey stars and cyan bars in Fig. 5c, d), but with relatively higher migration rates. This consistency across both the inter-model experiments from CMIP6 and the inter-member experiments from CESM1 LES indicates that faster equatorward migration rates are expected under future scenarios.

Discussions

The observed equatorward migration rates of the annual-mean HWL in the two hemispheres are equivalent, whereas there is a discrepancy in the CMIP6 historical experiments, which reveals an underestimation trend in HWL of the Northern Hemisphere; this may be due to the underestimated modulation of internal variability, to the underestimated response of heatwaves to external forcings, or to both, as quantitative assessments for underestimation require further study. The equatorward migration of HWL has already occurred in both hemispheres, as has the projected migration in future scenarios, suggesting increased heatwaves in presently warm regions, combining a 'warm-get-warmer' configuration. Any related changes in HWL latitude will have substantial impacts on human well-being and natural systems. The equatorward migration of HWL highlights that the risk of damage and disaster caused by heatwaves may increase at lower latitudes. Heatwaves also play essential roles in impacting droughts, agricultural security, wildfires, and ecosystems. In view of these motivating factors, further research on the equatorward trend of the HWL identified in this study, its regional and seasonal characteristics, and its potential linkage with the observed narrowing of the ITCZ is warranted.

Our result demonstrates the contribution of changes in soil moisture and ITCZ area in the HWL migration. The weakened contrast in soil moisture between tropics and subtropics and narrowing of ITCZ area provide conducive conditions for the equatorward migration of HWL. In addition, persistent changes in subtropical highs, jet streams, and stationary wave activity are known to influence heatwave formation and regional soil drying[43,44]. These dynamic features may alter the thermodynamic environment and amplify soil moisture anomalies and feedbacks. These processes are likely to interact and reinforce each other in complex ways, forming coupled feedbacks that modulate the spatial redistribution and shift in heatwave events. Understanding and quantifying the extent and dynamics of these interactions represents a key challenge for future research.

Further, it is documented that significant increases in the intensity, frequency, and duration of heatwaves under global warming[12,44]. In particular, the occurrence of long-duration heatwaves has been shown to increase nonlinearly with rising global temperatures[45]. Meanwhile, evident westward shift of mid-latitude heatwaves in the Northern Hemisphere are detected due to the intensified soil moisture–atmosphere coupling[46]. And also transboundary migrations of heatwaves across land and ocean regions is reported[47]. These works emphasized the zonal shift of heatwave events, our study discovered significant meridional migration of HWL at the hemispheric scale, offering insight into the latitudinal redistribution of present and future heat extremes. This perspective enhances our understanding of the geographic redistribution of heat risks under climate change, particularly in vulnerable lower latitude regions.

Methods

The reanalysis data

The analysis is mainly based on global daily maximum 2-m temperature (T_{max}) datasets from the European Centre for Medium-Range Weather Forecasts Reanalysis V5 (ERA5)[22], Climate Forecast System Reanalysis (CFSR)[23], Modern-Era Retrospective analysis for Research and Applications, Version 2 (MERRA2)[24], National Centers for Environment Prediction/National Center for Atmospheric Research (NCEP)[25], and Berkeley Earth grid surface temperature (Berkeley Earth)[26]. We also employ the global daily mean 2-m temperature (T_{mean}) as a reference to determine the usefulness of trends in T_{max}. All raw datasets are freely available for research application. We utilize the Volume of water in soil layer 1-2 data from the ERA5-Land dataset[48] to depict the global land soil moisture changes. Other atmospheric variables—mean surface direct shortwave radiation and total cloud cover—

https://doi.org/10.1038/s41467-025-63558-0

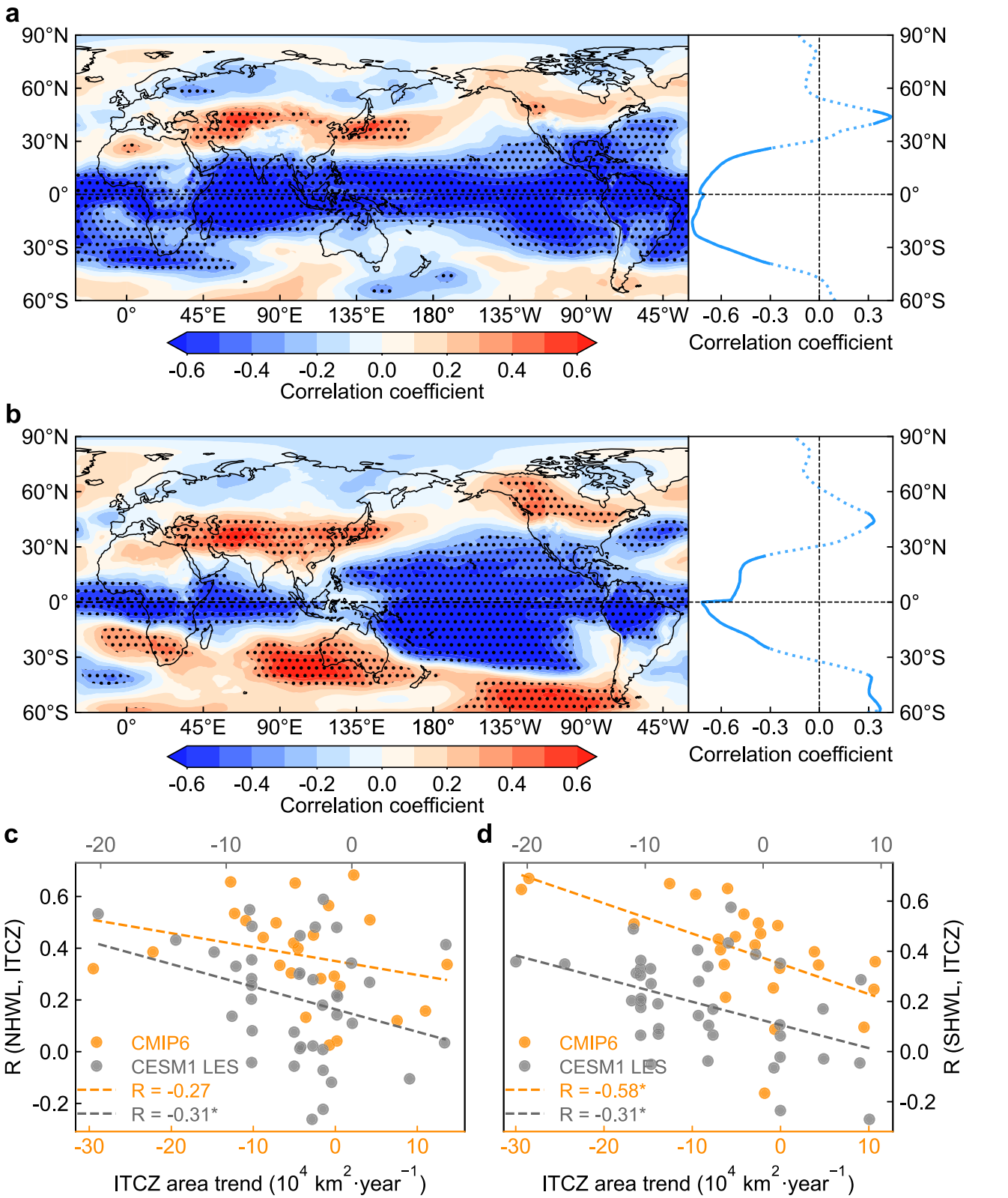

Fig. 3 | Physical mechanisms of intertropical convergence zone (ITCZ) contraction contribute to the equatorward migration of heatwave locations (HWL). a Spatial distribution of correlations between the time series of annual-mean latitude of HWL and static stability, and its zonal-mean profile. Annual-mean are taken over January-December in the Northern Hemisphere and July-June in the Southern Hemisphere. Dotted areas and solid line indicate statistical significance at the 0.05 level. **b** As in (**a**) but for correlations between the ITCZ area and static stability. **c**, **d** Intermodel scatterplot and linear fit of the ITCZ area trends ($km^2\ year^{-1}$) against the correlations between ITCZ area and HWL latitude in the Northern (**c**; NHWL) and Southern (**d**; SHWL) hemispheres calculated from CMIP6 (referenced to the bottom *x*-axis) and CESM1 LES (referenced to the top *x*-axis) historical simulations; with correlation coefficients shown in the bottom left corner, the asterisk indicates statistical significance at the 0.05 level. The CMIP6 models are selected based on their normalized root-mean-square error relative to ERA5; the specific models used are listed in the Supplementary Table 1.

https://doi.org/10.1038/s41467-025-63558-0

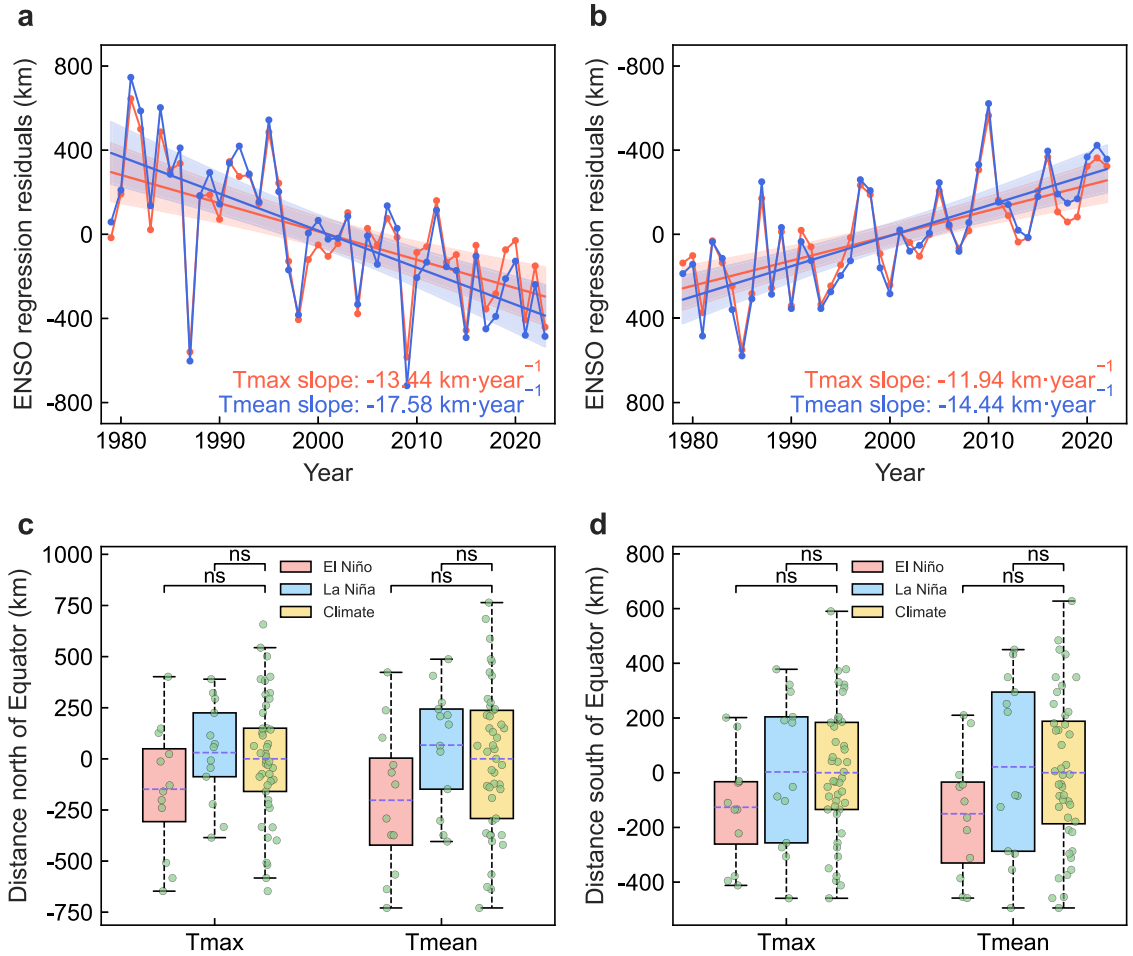

Fig. 4 | Impacts of El Niño–Southern Oscillation (ENSO) on the annual-mean latitude of heatwave locations (HWL). a, **b** Time series of annual-mean latitude of HWL with ENSO variability reduced in the Northern (**a**) and Southern (**b**) hemispheres. The values are calculated from residuals of the regression of ENSO variability against the HWL. The HWL is calculated from the ERA5 based on daily maximum 2-m temperature (T_{max}, red) and daily mean 2-m temperature (T_{mean}, blue). Linear trend lines are shown with their 95% two-sided confidence intervals (shaded). The slope (kilometres per year) significant at the 0.05 level is in colour. Negative slopes represent equatorward migration. The *y*-axis in (**b**) increases downwards. **c**, **d** Box plot for the annual-mean latitude of HWL during El Niño events (red), La Niña events (blue) and the whole period (yellow). The purple dashed lines indicate the average latitude of HWL in different cases. The '*ns*' indicates the differences between the connected two cases are non-significant at the 0.05 level based on Student's *t*-test and bootstrap testing.

are derived from the ERA5 reanalysis[22]. The common periods of the ERA5, CFSR, MERRA2, and NCEP datasets are compared over the post satellite era from 1979-2023, and the Berkeley Earth daily 2-m maximum (mean) temperature data are available from 1979-2022 (1979-2021). The annual-mean in the Southern Hemisphere is in accordance with the austral seasonal cycle; 1979 in the Southern Hemisphere refers to the average from July 1979 to June 1980 to guarantee a consecutive full austral summer. February 29th was removed from the leap year.

Only the land grid cells are examined by applying a land–sea mask to datasets based on natural Earth (https://www.naturalearthdata.com/). Antarctica was not considered when analysing the results for the Southern Hemisphere. The continents of Eurasia-North Africa and North America are divided by the Bering Strait.

CMIP6 models

We analysed daily maximum 2-m temperature from CMIP6 historical, hist-nat, hist-GHG, SSP3-7.0 and SSP5-8.5 experiments. For each experiment, the r1i1p1f1 member was analysed. The list of CMIP6 models used in each experiment is provided in Supplementary Table 1. The simulations during the periods 1979–2014 and 2065–2100 are used to compare the changes in the HWL trends between the historical and SSP3-7.0/SSP5-8.5 experiments. The mean seasonal cycles and reference periods in the SSP3-7.0 and SSP5-8.5 simulations are calculated from 2061 to 2090. The multimodel ensemble (MME) is the average annual-mean latitude of HWL from all the CMIP6 models, which can largely suppress the model spread and internal variability. All model outputs were re-gridded to a common 2° × 2° horizontal resolution via bilinear interpolation.

CESM1 LES

The CESM1 LES provides a valuable resource for investigating the roles of internal climate variability and external forcings under both historical and future scenarios[39]. We utilized the daily maximum 2-m temperature data from the CESM1 LES, which consists of 40 ensemble members that differ only in their initial atmospheric conditions while being subjected to the same external forcings; this enabled us to examine trends in the annual-mean latitude of HWL and evaluate the robustness of these trends across multiple simulations. For consistency in spatial analysis, all model outputs were re-gridded to a common 2° × 2° horizontal resolution via bilinear interpolation.

Removing the mean seasonal cycle

The mean seasonal cycle is calculated over 1981–2010 for each dataset and grid cell separately. The daily anomaly fields were calculated by removing the mean seasonal cycle before calculating the extreme threshold. The selection of the mean seasonal cycle would not

https://doi.org/10.1038/s41467-025-63558-0

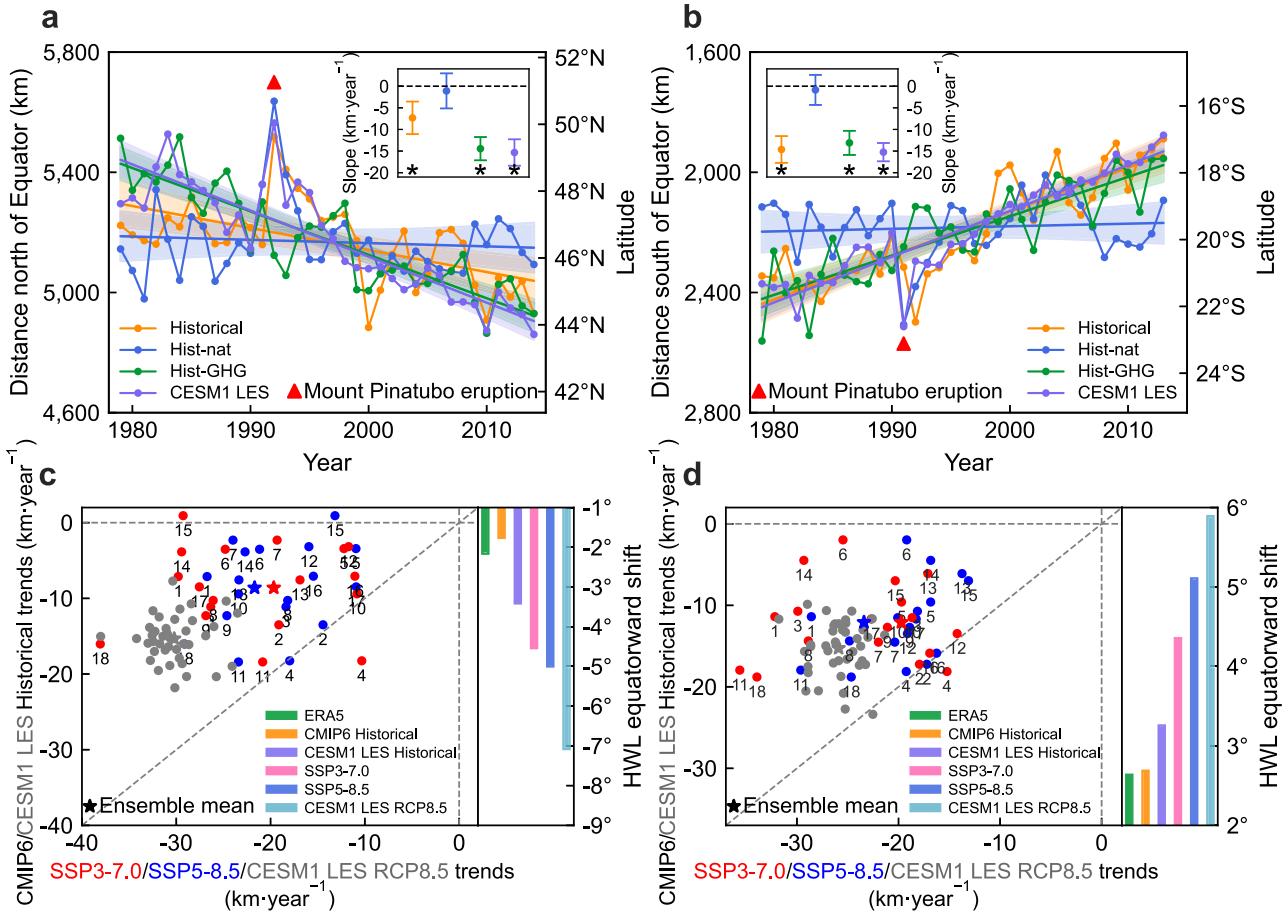

Fig. 5 | Simulated trends of annual-mean latitude of heatwave locations (HWL). **a**, **b** The multi-model ensemble (MME) time series (1979–2014) of the latitude of HWL calculated from the CMIP6 historical (orange lines), hist-nat (natural-only; blue lines), hist-GHG (GHG-only; green lines) and CESM1 LES (purple lines) experiments in the Northern (**a**) and Southern (**b**) hemispheres, with their irrespective slope and associated 95% two-sided confidence intervals in the upper corner. Shading indicates the 95% confidence intervals. The slope (kilometres per year) significant at the 0.05 level is marked with an asterisk. Negative slopes represent equatorward migration. The *y*-axis in (**b**) increases downwards. **c**, **d** Intermodel scatterplot of the HWL trends in the SSP3-7.0 (red), SSP5-8.5 (blue) and CESM1 LES RCP8.5 (grey) (during 2065–2100) against those in the CMIP6 and CESM1 LES historical (during 1979–2014) experiments for the Northern (**c**) and Southern (**d**) hemispheres, respectively. The trend for individual CMIP6 model (CESM1 member) expresses as colour (grey) circle (kilometres per year). The green bars represent the difference of average latitude of HWL between 2005–2014 and 1979–1988 from the ERA5 (referenced to the right *y*-axis). The orange, purple, pink, blue and cyan bars represent the differences of average latitude of HWL between the backmost ten-year and the beginning ten-year for CMIP6 historical, CESM1 LES historical, SSP3-7.0, SSP5-8.5 and CESM1 LES RCP8.5 experiments, respectively.

contaminate the equatorward migration of the annual-mean latitude of HWL. We recalculated the trends of the annual-mean HWL by taking 1961–1990 as the mean seasonal cycle and reference period[49], and the statistically significant equatorward migration rates in the two hemispheres remained and had similar magnitudes to those reported from 1981–2010 (Supplementary Fig. 12).

Annual-mean heatwave latitude and distance from the equator

The procedure adopted in this study for calculating the annual-mean latitude of HWL involves the following three steps:

(i) Identify the T_{max} (T_{mean}) extreme thresholds at a specific grid cell. The T_{max} (T_{mean}) thresholds are defined for each dataset and grid cell separately by calculating the 90th percentile over 30 years based on the daily T_{max} (T_{mean}). The 90th percentile threshold for each calendar day at each grid cell is determined from the distribution of multiyear samples of 5 days[50] (i.e., 2 days prior and 2 days after the given day with total samples: 5 days × 30 years = 150 days) over the reference period of 1981–2010.

(ii) The annual-mean latitude of HWL was identified. The heatwave events are defined on a grid-cell basis as at least 3 consecutive days that exceed the T_{max} (T_{mean}) extreme thresholds[49]. Therefore, the annual-mean latitude of heatwave events for year i is defined as follows:

$$\bar{\varphi}(i) = \frac{\sum_{m=1}^{M(i)} \varphi(i,m) \cdot N(i,m)}{\sum_{m=1}^{M(i)} N(i,m)} \quad (1)$$

where $\bar{\varphi}(i)$ is the average latitude of heatwave events for year i, $\varphi(i,m)$ denotes the latitude of heatwave events at grid m during year i, $N(i,m)$ represents the total number of heatwave events at grid cell m during year i, and $M(i)$ is the total grid number of heatwave events during year i

(iii) Converting the average latitude of HWL to the distance from the equator,

$$D(i) = R \times \left|\bar{\varphi}(i)\right| \times \frac{\pi}{180} \quad (2)$$

where $D(i)$ is the distance from the equator in kilometres for year i and R denotes the radius of the Earth, approximately 6371 km.

The annual-mean latitude of HWL represents the spatially averaged position of heatwaves rather than their actual geographic locations. Namely, a negative trend of HWL latitude refers an equatorward migration of the averaged HWL latitude, indicating that more frequent heatwaves occurrence at lower latitudes. The equatorward migration of the annual-mean latitude of HWL is not contaminated by the choice of extreme threshold. We recalculated the trends of the annual-mean HWL by taking the 95th percentile, and the significant equatorward migration rates in the two hemispheres remained and had similar magnitudes to those of the 90th percentile threshold (Supplementary Fig. 13).

Definition of ITCZ area and static stability

Following the method proposed by Michael P. Byrne et al.[19,41], the boundaries of the ITCZ are determined by the latitudes where the absolute value of the mass stream function (ψ) reaches its maximum on either side of the equator. Specifically, the ITCZ width is the distance between the northern and southern latitudes where the meridional derivative of the mass stream function, $\partial\psi/\partial\varphi$, equals zero. The ITCZ area is calculated as follows:

$$A_{ITCZ} = 2\pi R^2(\sin\varphi_n - \sin\varphi_s) \quad (3)$$

where R is the radius of the Earth, and φ_n and φ_s are the latitudes of the northern and southern boundaries of the ITCZ, respectively.

The static stability is defined as the vertical potential temperature gradient ($\Delta\theta/\Delta z$) between the 250 hPa (upper troposphere) and 850 hPa (lower troposphere), a key metric of atmospheric stratification.

Definition of soil moisture difference (SMD)

To investigate the influence of latitudinal contrast in soil moisture on the HWL latitude, we define a soil moisture difference (SMD) index to characterize the meridional contrast in soil moisture across different latitude bands, as follows:

$$SMD = SM[15^\circ S - 15^\circ N] - 0.5 \times (SM[30^\circ S - 15^\circ S] + SM[15^\circ N - 30^\circ N]) \quad (4)$$

where '[]' denotes the latitude-weighted areal mean. This index reflects the difference in soil moisture between the tropics (15°S–15°N) and subtropics (30°–15°S and 15°–30°N). Additionally, similar result is observed using 20° to separate the tropics and subtropics, confirming the robustness of the SMD definition.

Removing the ENSO variability

ENSO variability was removed from the annual-mean heatwave latitude time series by regressing the individual series from the Northern and Southern hemispheres onto the Niño 3.4 index and analysing the residuals. The Niño 3.4 index is downloaded via https://psl.noaa.gov/gcos_wgsp/Timeseries/Data/nino34.long.data. With respect to the Northern Hemisphere, the effect of the previous mature boreal winter (December (-1) to February (0)) Niño 3.4 index is used to verify the potential impacts of ENSO variability. The simultaneous effect of the mature season Niño 3.4 index is detected in the Southern Hemisphere. This method assumes a linear relationship between the HWL latitudes and ENSO and that the Niño 3.4 index captures all of the ENSO signals. Both assumptions lead to an imperfect model; therefore, residual ENSO may remain in the data.

Definitions of El Niño and La Niña events

The Niño 3.4 index is used to identify El Niño and La Niña events, https://origin.cpc.ncep.noaa.gov/products/analysis_monitoring/ensostuff/ONI_v5.php. It is calculated as the 3 month running mean of sea surface temperature anomalies in the Niño 3.4 region (5°S–5°N, 120°W–170°W). An El Niño event is defined when the Niño 3.4 index exceeds +0.5 °C for at least six consecutive months, whereas a La Niña event is defined when it remains below -0.5 °C for at least six consecutive months. Consequently, twelve El Niño events (1982/83, 1986/87, 1987/88, 1991/92, 1994/95, 1997/98, 2002/03, 2004/05, 2009/10, 2014/15, 2015/16, 2018/19) and thirteen La Niña events (1984/85, 1988/89, 1995/96, 1998/99, 1999/2000, 2000/01, 2007/08, 2010/11, 2011/12, 2017/18, 2020/21, 2021/22, 2022/23) are selected.

Statistics test

Statistical significance was computed at the 0.05 level via Student's *t*-test. The linear trend is calculated based on the ordinary least squares and the Theil–Sen estimator[51,52], and is tested via Student's *t*-test and Mann-Kendall test. None of the time series explored in this study exhibited autocorrelations after detrending, as determined with the Durbin–Watson test statistic[53–55]. In addition, to evaluate the relationship between the HWL latitude and atmospheric variables, we conducted correlation analyses. Specifically, the correlations between the time series of annual-mean latitude of HWL and atmospheric variables (e.g., soil moisture, static stability) are calculated separately for the Northern and Southern hemispheres.

Data availability

The ERA5 and ERA5-Land reanalysis data[22,48] are available at https://www.ecmwf.int/en/forecasts/dataset/ecmwf-reanalysis-v5 and https://doi.org/10.24381/cds.68d2bb30. The CFSR data[23] can be downloaded from https://rda.ucar.edu/datasets/. The MERRA2 data[24] are obtained from https://disc.gsfc.nasa.gov/datasets?project=MERRA-2. The NCEP data[25] can be accessible through https://psl.noaa.gov/data/gridded/. The Berkeley Earth data[26] are downloaded from https://berkeleyearth.org/data/. The outputs of CMIP6 simulations can be downloaded from the following website: https://esgf-node.ipsl.upmc.fr/search/cmip6-ipsl/. The CESM1 LES data[39] are available at https://rda.ucar.edu/datasets/d651027/. The raw data to generate the main figures in this study are available at Code Ocean under the identifier https://doi.org/10.24433/CO.5427449.v3[56].

Code availability

The main code for this study can be downloaded from Code Ocean at https://doi.org/10.24433/CO.5427449.v3[56].

References

1. Coumou, D. & Rahmstorf, S. A decade of weather extremes. *Nat. Clim. Change* **2**, 491–496 (2012).
2. Perkins, S. E. & Alexander, L. V. On the measurement of heat waves. *J. Clim.* **26**, 4500–4517 (2013).
3. Wouters, H. et al. Soil drought can mitigate deadly heat stress thanks to a reduction of air humidity. *Sci. Adv.* **8**, eabe6653 (2022).
4. Bureau of Meteorology. *Special Climate Statement 68—widespread Heatwaves During December 2018 And January 2019*. http://www.bom.gov.au/climate/current/statements/scs68.pdf (2019).
5. Sousa, P. M. et al. Distinct influences of large-scale circulation and regional feedbacks in two exceptional 2019 European heatwaves. *Commun. Earth Environ.* **1**, 1–13 (2020).
6. Aadhar, S. & Mishra, V. The 2022 mega heatwave in South Asia in the observed and projected future climate. *Environ. Res. Lett.* **18**, 104011 (2023).
7. Tang, S. et al. Linkages of unprecedented 2022 Yangtze river valley heatwaves to Pakistan flood and triple-dip La Niña. *npj Clim. Atmos. Sci.* **6**, 1–8 (2023).
8. Perkins-Kirkpatrick, S. et al. Extreme terrestrial heat in 2023. *Nat. Rev. Earth Environ.* **5**, 244–246 (2024).
9. IFRC. *Deadly Heatwave In The Sahel And West Africa Would Have Been Impossible Without Human-caused Climate Change*. https://www.ifrc.org/nota-prensa/deadly-heatwave-sahel-and-west-

africa-would-have-been-impossible-without-human-caused (2024).
10. Meehl, G. A. & Tebaldi, C. More intense, more frequent, and longer lasting heat waves in the 21st century. *Science* **305**, 994–997 (2004).
11. Rasmijn, L. M. et al. Future equivalent of 2010 Russian heatwave intensified by weakening soil moisture constraints. *Nat. Clim. Change* **8**, 381–385 (2018).
12. Perkins-Kirkpatrick, S. E. & Lewis, S. C. Increasing trends in regional heatwaves. *Nat. Commun.* **11**, 3357 (2020).
13. McEvoy, D. J. & Hatchett, B. J. Spring heat waves drive record western United States snow melt in 2021. *Environ. Res. Lett.* **18**, 014007 (2023).
14. Wu, S. et al. Season-dependent heatwave mechanisms: a study of southern China. *Weather Clim. Extremes* **42**, 100603 (2023).
15. Lemus-Canovas, M., Insua-Costa, D., Trigo, R. M. & Miralles, D. G. Record-shattering 2023 spring heatwave in western mediterranean amplified by long-term drought. *npj Clim. Atmos. Sci.* **7**, 1–8 (2024).
16. Seidel, D. J., Fu, Q., Randel, W. J. & Reichler, T. J. Widening of the tropical belt in a changing climate. *Nat. Geosci.* **1**, 21–24 (2008).
17. Scheff, J. & Frierson, D. M. W. Robust future precipitation declines in CMIP5 largely reflect the poleward expansion of model subtropical dry zones. *Geophys. Res. Lett.* https://doi.org/10.1029/2012GL052910 (2012).
18. Kossin, J. P., Emanuel, K. A. & Vecchi, G. A. The poleward migration of the location of tropical cyclone maximum intensity. *Nature* **509**, 349–352 (2014).
19. Byrne, M. P. & Schneider, T. Narrowing of the ITCZ in a warming climate: physical mechanisms. *Geophys. Res. Lett.* **43**, 11,350–11,357 (2016).
20. Zhou, W., Xie, S.-P. & Yang, D. Enhanced equatorial warming causes deep-tropical contraction and subtropical monsoon shift. *Nat. Clim. Chang.* **9**, 834–839 (2019).
21. Liu, Y., Cai, W., Lin, X. & Li, Z. Increased extreme swings of Atlantic intertropical convergence zone in a warming climate. *Nat. Clim. Chang.* **12**, 828–833 (2022).
22. Hersbach, H. et al. The ERA5 global reanalysis. *Q. J. R. Meteorol. Soc.* **146**, 1999–2049 (2020).
23. Saha, S. et al. *NCEP Climate Forecast System Reanalysis (CFSR) 6-hourly Products, January 1979 to December 2010*. https://cmr.earthdata.nasa.gov/search/concepts/C1214110933-SCIOPS.html (2010).
24. Gelaro, R. et al. The modern-era retrospective analysis for research and applications, version 2 (MERRA-2). *J. Clim.* **30**, 5419–5454 (2017).
25. Kalnay, E. et al. The NCEP/NCAR 40 year reanalysis project. *Bull. Am. Meteorol. Soc.* **77**, 437–472 (1996).
26. Rohde, R. A. & Hausfather, Z. The berkeley earth land/ocean temperature record. *Earth Syst. Sci. Data* **12**, 3469–3479 (2020).
27. Kent, S. T., McClure, L. A., Zaitchik, B. F., Smith, T. T. & Gohlke, J. M. Heat waves and health outcomes in alabama (USA): the importance of heat wave definition. *Environ. Health Perspect.* **122**, 151–158 (2014).
28. Ma, W. et al. The short-term effect of heat waves on mortality and its modifiers in China: an analysis from 66 communities. *Environ. Int.* **75**, 103–109 (2015).
29. Xu, Z., FitzGerald, G., Guo, Y., Jalaludin, B. & Tong, S. Impact of heatwave on mortality under different heatwave definitions: a systematic review and meta-analysis. *Environ. Int.* **89–90**, 193–203 (2016).
30. Zhou, S., Yu, B. & Zhang, Y. Global concurrent climate extremes exacerbated by anthropogenic climate change. *Sci. Adv.* **9**, eabo1638 (2023).
31. Cai, W. et al. Pantropical climate interactions. *Science* **363**, eaav4236 (2019).
32. Wang, C. Three-ocean interactions and climate variability: a review and perspective. *Clim. Dyn.* **53**, 5119–5136 (2019).
33. Knight, J. R., Folland, C. K. & Scaife, A. A. Climate impacts of the Atlantic multidecadal oscillation. *Geophys. Res. Lett.* https://doi.org/10.1029/2006GL026242 (2006).
34. Hari, V., Ghosh, S., Zhang, W. & Kumar, R. Strong influence of north Pacific Ocean variability on Indian summer heatwaves. *Nat. Commun.* **13**, 5349 (2022).
35. Wei, J., Han, W., Wang, W., Zhang, L. & Rajagopalan, B. Intensification of heatwaves in China in recent decades: Roles of climate modes. *npj Clim. Atmos. Sci.* **6**, 1–12 (2023).
36. Zhang, P. et al. Abrupt shift to hotter and drier climate over inner East Asia beyond the tipping point. *Science* **370**, 1095–1099 (2020).
37. Zhang, X. et al. Increased impact of heat domes on 2021-like heat extremes in North America under global warming. *Nat. Commun.* **14**, 1690 (2023).
38. Qiao, L. et al. Soil moisture–atmosphere coupling accelerates global warming. *Nat. Commun.* **14**, 4908 (2023).
39. Kay, J. E. et al. The community earth system model (CESM) large ensemble project: a community resource for studying climate change in the presence of internal climate variability. *Bull. Am. Meteorol. Soc.* **96**, 1333–1349 (2015).
40. Wodzicki, K. R. & Rapp, A. D. Long-term characterization of the Pacific ITCZ using TRMM, GPCP, and ERA-interim. *J. Geophys. Res. Atmos.* **121**, 3153–3170 (2016).
41. Byrne, M. P. & Schneider, T. Energetic constraints on the width of the intertropical convergence zone. *J. Clim.* **29**, 4709–4721 (2016).
42. Loughran, T. F., Pitman, A. J. & Perkins-Kirkpatrick, S. E. The El Niño–Southern oscillation's effect on summer heatwave development mechanisms in Australia. *Clim. Dyn.* **52**, 6279–6300 (2019).
43. Teng, H., Branstator, G., Wang, H., Meehl, G. A. & Washington, W. M. Probability of US heat waves affected by a subseasonal planetary wave pattern. *Nat. Geosci.* **6**, 1056–1061 (2013).
44. Perkins, S. E. A review on the scientific understanding of heatwaves—their measurement, driving mechanisms, and changes at the global scale. *Atmos. Res.* **164–165**, 242–267 (2015).
45. Martinez-Villalobos, C., Fu, D., Loikith, P. C. & Neelin, J. D. Accelerating increase in the duration of heatwaves under global warming. *Nat. Geosci.* **18**, 716–723 (2025).
46. Zhang, K., Zuo, Z., Mei, W., Zhang, R. & Dai, A. A westward shift of heatwave hotspots caused by warming-enhanced land–air coupling. *Nat. Clim. Chang.* **15**, 546–553 (2025).
47. Gu, X. et al. Frequent land-ocean transboundary migration of tropical heatwaves under climate change. *Nat. Commun.* **16**, 3400 (2025).
48. Muñoz Sabater, J. *ERA5-Land Monthly Averaged Data From 1950 to Present*. https://cds.climate.copernicus.eu/datasets/reanalysis-era5-land?tab=overview (2019).
49. Brunner, L. & Voigt, A. Pitfalls in diagnosing temperature extremes. *Nat. Commun.* **15**, 2087 (2024).
50. Zhang, X., Hegerl, G., Zwiers, F. W. & Kenyon, J. Avoiding inhomogeneity in percentile-based indices of temperature extremes. *J. Clim.* **18**, 1641–1651 (2005).
51. Gocic, M. & Trajkovic, S. Analysis of changes in meteorological variables using Mann-Kendall and Sen's slope estimator statistical tests in Serbia. *Glob. Planet. Change* **100**, 172–182 (2013).
52. Virtanen, P. et al. SciPy 1.0: fundamental algorithms for scientific computing in python. *Nat. Methods* **17**, 261–272 (2020).
53. Durbin, J. & Watson, G. S. Testing for serial correlation in least squares regression: I. *Biometrika* **37**, 409–428 (1950).
54. Durbin, J. & Watson, G. S. Testing for serial correlation in least squares regression. *Ii. Biometrika* **38**, 159–177 (1951).

55. Seabold, S. & Perktold, J. Statsmodels: Econometric and Statistical Modeling with Python. In *Proceedings of the 9th Python in Science Conference* (eds. van der Walt, S. & Millman, J.) 92–96 (2010).
56. Feng, J., Li, J., Jin, F.-F., Zhao, S. & Li, J. Figure code and data of 'Anthropogenic forcing drives equatorward migration of heatwave locations across continents'. https://doi.org/10.24433/CO.5427449.v3 (2025).

Acknowledgements

This work was supported by the National Natural Science Foundation of China (42222501) (F.J.), the National Key Research and Development Program of China (2023YFF0805100) (L.J.P. and F.J.), the National Natural Science Foundation of China (42475021) (F.J.), the Fundamental Research Funds for the Central Universities (2233300001 and 2024-KYTD-02) (F.J.), and the Joint Research Project for Meteorological Capacity Improvement (24NLTSZ005) (F.J.).

Author contributions

J.F. and J.P.L. conceptualized the research. J.X.L. produced the figures. J.F. conducted the analysis and wrote the initial manuscript, in discussion with F.-F.J., J.P.L. and S.Z. J.F., J.X.L. and J.P.L. structured the paper. All authors contributed to interpreting the results and improving the paper.

Competing interests

The authors declare no competing interests.

Additional information

Supplementary information The online version contains supplementary material available at https://doi.org/10.1038/s41467-025-63558-0.

Correspondence and requests for materials should be addressed to Juan Feng or Jianping Li.

Peer review information *Nature Communications* thanks Marc Lemus-Canovas and the other, anonymous, reviewer for their contribution to the peer review of this work. A peer review file is available.